Check for updates

RESEARCH ARTICLE

NANO · MICRO small
www.small-journal.com

Antiferroelectricity-Induced Negative Thermal Expansion in Double Perovskite Pb_2CoMoO_6

Haoting Zhao, Zhao Pan, Xi Shen, Jianfa Zhao, Dabiao Lu, Jie Zhang, Zhiwei Hu, Chang-Yang Kuo, Chien-Te Chen, Ting-Shan Chan, Christoph J. Sahle, Cheng Dong, Takumi Nishikubo, Takehiro Koike, Zun-Yi Deng, Jiawang Hong, Runze Yu, Pu Yu, Masaki Azuma, Changqing Jin, and Youwen Long**

Materials with negative thermal expansion (NTE) attract significant research attention owing to their unique physical properties and promising applications. Although ferroelectric phase transitions leading to NTE are widely investigated, information on antiferroelectricity-induced NTE remains limited. In this study, single-crystal and polycrystalline Pb_2CoMoO_6 samples are prepared at high pressure and temperature conditions. The compound crystallizes into an antiferroelectric *Pnma* orthorhombic double perovskite structure at room temperature owing to the opposite displacements dominated by Pb^{2+} ions. With increasing temperature to 400 K, a structural phase transition to cubic *Fm*-3*m* paraelectric phase occurs, accompanied by a sharp volume contraction of 0.41%. This is the first report of an antiferroelectric-to-paraelectric transition-induced NTE in Pb_2CoMoO_6. Moreover, the compound also exhibits remarkable NTE with an average volumetric coefficient of thermal expansion $\alpha_V = -1.33 \times 10^{-5}$ K^{-1} in a wide temperature range of 30–420 K. The as-prepared Pb_2CoMoO_6 thus serves as a prototype material system for studying antiferroelectricity-induced NTE.

1. Introduction

Negative thermal expansion (NTE) materials have attracted extensive attention in recent decades owing to their intriguing physical properties and potential applications in optical instruments, precise machining equipment, advanced electronics, fuel cells, etc.[1] Compared to materials that generally exhibit positive thermal expansion (PTE) arising from the anharmonic vibration of atoms, NTE materials exhibit counterintuitive thermal shrinkage upon heating, that is, the coefficient of thermal expansion is negative. As a result, NTE materials can be used to counteract thermal expansion by forming composites with PTE materials or to realize controllable thermal expansion in single-phase materials via chemical substitution to obtain zero thermal expansion (ZTE)

H. Zhao, Z. Pan, X. Shen, J. Zhao, D. Lu, J. Zhang, C. Jin, Y. Long
Beijing National Laboratory for Condensed Matter Physics
Institute of Physics
Chinese Academy of Sciences
Beijing 100190, China
E-mail: ywlong@iphy.ac.cn

H. Zhao
College of Materials Science and Opto-Electronic Technology
University of Chinese Academy of Sciences
Beijing 100049, China

J. Zhao, D. Lu, J. Zhang, C. Jin, Y. Long
School of Physical Sciences
University of Chinese Academy of Sciences
Beijing 100049, China

Z. Hu
Max Planck Institute for Chemical Physics of Solids
01187 Dresden, Germany

C.-Y. Kuo
Department of Electrophysics
National Yang Ming Chiao Tung University
Hsinchu 30010, Taiwan

C.-Y. Kuo, C.-T. Chen, T.-S. Chan
National Synchrotron Radiation Research Center
Hsinchu 30076, Taiwan

C. J. Sahle
European Synchrotron Radiation Facility (ESRF)
71 Avenue des Martyrs, Grenoble 38000, France

C. Dong
School of Advanced Materials
Peking University Shenzhen Graduate School
Shenzhen 518055, China

T. Nishikubo, M. Azuma
Kanagawa Institute of Industrial Science and Technology
Ebina 243–0435, Japan

T. Nishikubo, T. Koike, M. Azuma
Laboratory for Materials and Structures
Institute of Innovative Research
Tokyo Institute of Technology
Yokohama 226–8503, Japan

Z.-Y. Deng, J. Hong
School of Aerospace Engineering
Beijing Institute of Technology
Beijing 100081, China

The ORCID identification number(s) for the author(s) of this article can be found under https://doi.org/10.1002/smll.202305219

DOI: 10.1002/smll.202305219

 © 2023 Wiley-VCH GmbH

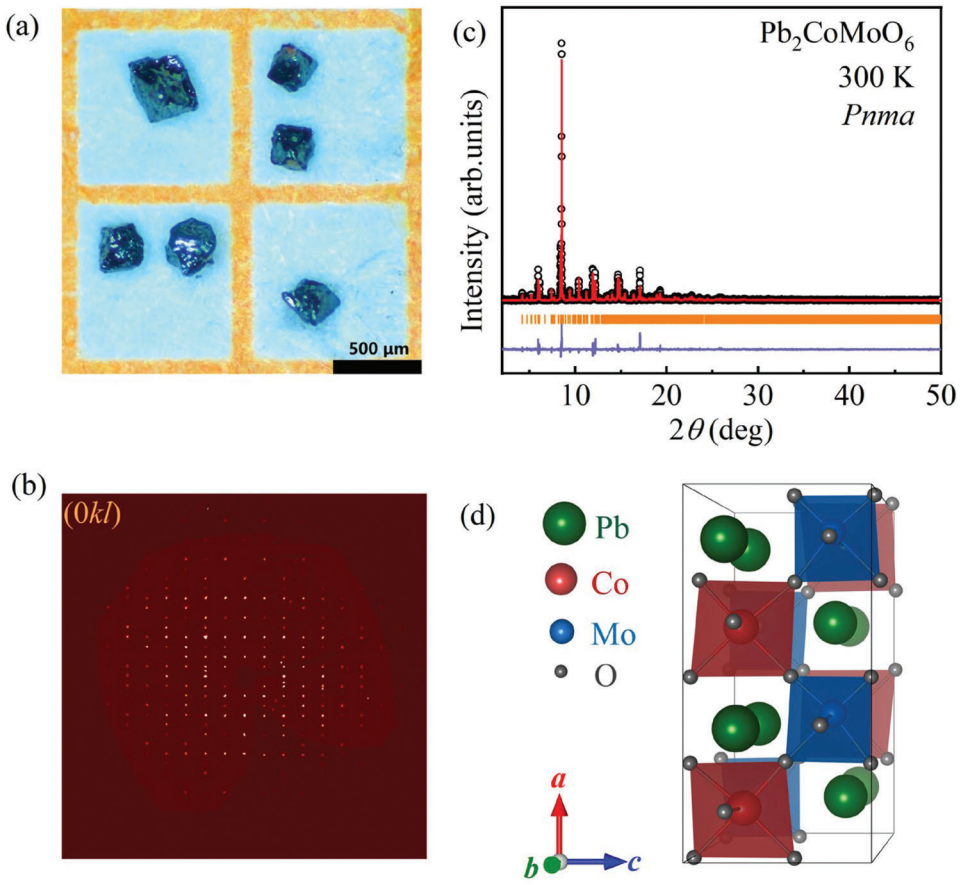

Figure 1. a) Photographs of Pb_2CoMoO_6 single crystals. b) Representative single-crystal XRD image for the 0*kl* reciprocal lattice plane. c) Powder SXRD pattern and refinement results obtained at 300 K. Observed (black circle), calculated (red line), and difference (purple line) values are shown. Orange ticks indicate the allowed Bragg reflections. d) Schematic crystal structure of Pb_2CoMoO_6 with the *Pnma* space group, in which the corner-sharing CoO_6 and MoO_6 octahedra are shown.

materials.[1a,2] The average volumetric coefficient of thermal expansion can be defined as $\alpha_V = \Delta V/(V_0 \times \Delta T)$, where V_0 is the initial volume and ΔV is the volume change corresponding to the temperature change ΔT.

R. Yu
Center for High-Pressure Science and Technology Advanced Research
Beijing 100094, China
E-mail: runze.yu@hpstar.ac.cn
P. Yu
State Key Laboratory of Low Dimensional Quantum Physics
Department of Physics
Tsinghua University
Beijing 100084, China
M. Azuma
Living Systems Materialogy (LiSM) Research Group
International Research Frontiers Initiative (IRFI)
Tokyo Institute of Technology
4259, Nagatsuta-cho, Midori-ku, Yokohama 226–8501, Japan
C. Jin, Y. Long
Songshan Lake Materials Laboratory
Dongguan 523808, China

Although materials with unconventional thermal expansion have developed rapidly in recent years, the number of single-phase NTE materials is limited.[3] Therefore, the development of new materials with novel NTE mechanisms is essential. Thus far, the underlying mechanisms of NTE mainly include phonon-related transverse vibrations and rigid unit models as observed in ZrW_2O_8 and $Fe[Co(CN)_6]$ frameworks,[1f,4] the magnetovolume effects as demonstrated in Invar alloys,[5] the ferroelectric effect as presented in $PbTiO_3$-based and $PbVO_3$-based ferroelectrics,[6] and the changes in the electronic state as noted in $BiNiO_3$, $LaCu_3Fe_4O_{12}$, and V_2OPO_4.[7] Among them, ferroelectricity-induced NTE, which can be quantitatively described by spontaneous volume ferroelectrostriction, has been widely studied.[8] Generally, NTE occurs during the ferroelectric-to-paraelectric or ferroelectric-to-antiferroelectric phase transitions, whereas it is not observed during an antiferroelectric-to-paraelectric phase transition.[9] In this study, an antiferroelectric double perovskite oxide Pb_2CoMoO_6 was prepared using high-pressure synthesis techniques. The antiferroelectric phase was found to change into a paraelectric phase upon heating to ≈400 K, leading to a significant volume shrinking of 0.41%. This is the first report of an antiferroelectric-to-paraelectric transition-induced NTE in Pb_2CoMoO_6. Moreover, the compound also exhibits remarkable

© 2023 Wiley-VCH GmbH

16136829, 2024, 2, Downloaded from https://onlinelibrary.wiley.com/doi/10.1002/smll.202305219 by Institute Of Physics Chinese Academy Of Sciences, Wiley Online Library on [16/04/2024]. See the Terms and Conditions (https://onlinelibrary.wiley.com/terms-and-conditions) on Wiley Online Library for rules of use; OA articles are governed by the applicable Creative Commons License

NTE with an average volumetric coefficient of thermal expansion of $\alpha_V = -1.33 \times 10^{-5}$ K^{-1} in a wide temperature region of 30–420 K.

2. Results and Discussion

2.1. Crystal Structure of Pb_2CoMoO_6

Although the synthesis of polycrystalline Pb_2CoMoO_6 powder was reported in the 1970s,[10] the crystal structures and physical properties have not been studied in detail. In this study, the crystal structure of Pb_2CoMoO_6 at room temperature (RT) was determined using both single-crystal X-ray diffraction (XRD) and powder synchrotron X-ray diffraction (SXRD) methods. This is the first time that Pb_2CoMoO_6 single crystals have been grown under high-pressure conditions; photographs of the crystals are shown in **Figure 1**a. The crystals were typically 200 μm in size with an octahedral shape. Figure 1b shows a representative single-crystal XRD pattern of the 0*kl* reciprocal lattice plane. Sharp diffraction spots were observed without visible spallation, and all the spots were well-indexed based on an orthorhombic symmetry, suggesting the high quality of the single crystals. Single-crystal structural analysis revealed that Pb_2CoMoO_6 crystallized into a double perovskite structure with a *Pnma* space group (No. 62). The lattice parameters were $a_{orth.} = 11.4401(6)$, $b_{orth.} = 7.9204(4)$, and $c_{orth.} = 5.7030(3)$ Å. In the *Pnma* symmetry, Pb atoms occupied the 8*d* (*x*, *y*, *z*) Wyckoff site, and Co and Mo atoms occupied the 4*c* (*x*, 0.75, *z*) and 4*c* (*x*, 0.25, *z*) sites, respectively, forming a B-site-ordered distribution. In addition, the O atoms occupied five different Wyckoff sites, including four 4*c* sites and one 8*d* site. The detailed crystallographic data, including atomic coordinates, bond lengths, and angles obtained from single-crystal XRD measurements, are summarized in **Tables 1** and **2**, and S1, Supporting Information. Based on the bond lengths, bond valence sum (BVS) calculations revealed the charge combination as $Pb^{2+}{}_2Co^{2+}Mo^{6+}O_6$ (Table S1, Supporting Information), which was consistent with the X-ray absorption spectroscopy results (Figure S1, Supporting Information). Figure 1c shows the powder SXRD pattern of Pb_2CoMoO_6 measured at 300 K and the related structural refinement results. The refined structural parameters (Tables S2 and S3, Supporting Information) agreed well with those obtained using single-crystal XRD analysis. The crystal structure of the B-site-ordered Pb_2CoMoO_6 is shown in Figure 1d. The CoO_6 and MoO_6 octahedra shared corners and were alternately distributed along the [102] and [010] directions, whereas the Pb atoms were located in the voids surrounded by the octahedra.

$$R1 = \sum \| F_o | - | F_c \| / \left| \sum F_o \right|, wR_2 = \left[\sum w\left(F_o^2 - F_c^2\right)^2 / \sum \left(F_o^2\right)^2 \right]^{1/2} \quad (1)$$

2.2. Structural and Lattice Evolutions of Pb_2CoMoO_6

To determine the structural stability, temperature-dependent differential scanning calorimetry (DSC) was performed on Pb_2CoMoO_6. **Figure 2**a depicts the DSC data between RT and 470 K for both the heating and cooling processes. With increasing temperature, an endothermic peak emerged at 400 K, passing the minimum at 410 K. However, during cooling, the exothermic peak maximum occurred at 399 K. Such distinct heat hysteresis is indicative of a first-order structural phase transition.[11] Temperature-variable SXRD was further measured

Table 1. Crystallographic data of Pb_2CoMoO_6 determined by single-crystal XRD at 300 K.

Parameter	Value	Parameter	Value
Chemical formula	Pb_2CoMoO_6	D_{cal} [g cm^{-3}]	8.551
Formula weight [g mol^{-1}]	665.25	F(000)	1124
Temperature [K]	300(2)	Theta range [°]	3.56–28.26
Wavelength [Å]	0.71073	Reflections collected	5169
Crystal size [mm]	0.080 × 0.100 × 0.150	Independent reflections	681 [R(int) = 0.0585]
Crystal system	orthorhombic	Coverage of independent reflections	99.6%
Space group	*Pnma*	Goodness-of-fit on F^2	1.116
a [Å]	11.4401(6)	Final R indices	619 data; I > 2σ(I) R1 = 3.74%, wR2 = 9.83%[a]
b [Å]	7.9204(4)		All data R1 = 3.92%, wR2 = 9.98%
c [Å]	5.7030(3)	Largest diff. peak and hole [eÅ^{-3}]	1.892 and −4.753
Volume [Å^3]	516.75(5)	R.M.S. deviation from mean [eÅ^{-3}]	0.781
Z	4		

[a] Equation (1).

Table 2. Atomic coordinates and equivalent isotropic atomic displacement parameters of Pb_2CoMoO_6 determined by single-crystal XRD at 300 K.

Atom	Site	*x*	*y*	*z*	$100 \times U_{iso}$ [Å^2]
Pb	8*d*	0.64554 (4)	0.49428 (4)	0.71942 (9)	1.96 (2)
Co	4*c*	0.6230 (2)	0.75	0.2490 (3)	0.72 (4)
Mo	4*c*	0.6135 (1)	0.25	0.2447 (2)	0.85 (3)
O1	4*c*	0.5035 (8)	0.25	0.488 (2)	2.1 (2)
O2	4*c*	0.7501 (7)	0.75	0.540 (2)	1.5 (2)
O3	4*c*	0.7376 (8)	0.25	0.528 (2)	1.6 (2)
O4	4*c*	0.4904 (8)	0.75	0.991 (1)	1.7 (2)
O5	8*d*	0.6330 (9)	0.4885 (8)	0.273 (2)	1.9 (2)

© 2023 Wiley-VCH GmbH

16136829, 2024, 2, Downloaded from https://onlinelibrary.wiley.com/doi/10.1002/smll.202305219 by Institute Of Physics Chinese Academy Of Sciences, Wiley Online Library on [16/04/2024]. See the Terms and Conditions (https://onlinelibrary.wiley.com/terms-and-conditions) on Wiley Online Library for rules of use; OA articles are governed by the applicable Creative Commons License

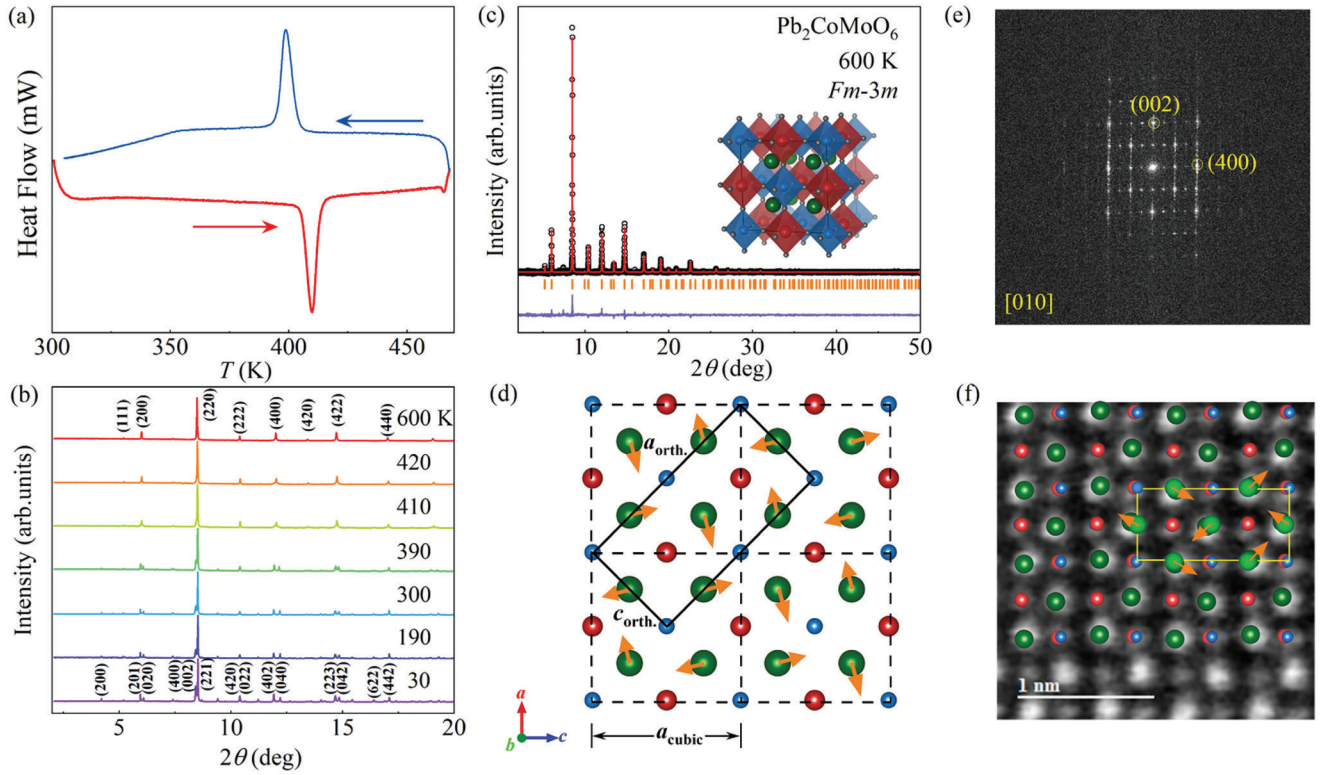

Figure 2. a) Temperature dependence of heat flow obtained via DSC for Pb_2CoMoO_6. b) Representative SXRD patterns obtained between 30 and 600 K. c) Powder SXRD pattern and refinement results obtained at 600 K. Observed (black circle), calculated (red line), and difference (purple line) values are shown. Orange ticks indicate the allowed Bragg reflections. Inset shows the crystal structure of Pb_2CoMoO_6 with the *Fm*-3*m* space group. d) Schematic Pb^{2+} atomic displacements in the *ac* plane for Pb_2CoMoO_6. Solid and dashed lines indicate the orthorhombic and cubic unit cells, respectively. e) The FFT of the HAADF image and f) the HAADF image along the [010] zone axis. Structural schematics are overlaid in (f). Olive, red, and blue balls represent Pb, Co, and Mo atoms, respectively. Matte green balls in (f) represent Pb atoms in the cubic phase. Arrows indicate the direction of Pb displacements.

from 30 to 600 K to study the structural and lattice evolutions of Pb_2CoMoO_6. As shown in Figure 2b, when the temperature increases from 30 to 390 K, no significant variations were observed in the diffraction peaks, suggesting the stability of crystal structure in this temperature region. However, above 390 K, the SXRD patterns changed significantly. In particular, the initially separated orthorhombic reflections merged to form single reflections. For example, the well-separated 201 and 020, 402 and 040, and 223 and 042 peaks changed into single 200, 400, and 422 peaks, respectively. These features revealed the occurrence of a structural phase transition toward a higher crystal symmetry. As shown in Figure 2c, Rietveld analysis based on the SXRD pattern collected at 600 K demonstrated that Pb_2CoMoO_6 exhibited a cubic perovskite structure with the space group *Fm*-3*m* (No. 225) and refined lattice parameter a_{cubic} = 8.02700(6) Å. In this crystal symmetry, the Pb, Co, and Mo atoms occupied the special Wyckoff sites 8*c* (0.25, 0.25, 0.25), 4*b* (0.5, 0.5, 0.5), and 4*a* (0, 0, 0), respectively. The O atoms occupied the Wyckoff site 24*e* (*x*, 0, 0). The detailed structural parameters refined at 600 K are presented in **Tables 3** and S4, Supporting Information. Based on the BVS calculations (Table S4, Supporting Information), the cation charge states in the high-temperature cubic phase were similar to those of the low-temperature orthorhombic phase, eliminating the possibility of the occurrence of intermetallic charge transfer, as observed in other perovskite oxides, such as $LaCu_3Fe_4O_{12}$ and $BiNiO_3$.[7a,b] Notably, two phases coexisted at 400 and 410 K in Pb_2CoMoO_6, which was in agreement with the first-order characteristics of the phase transition determined via DSC. Moreover, the structural phase transition is reversible (see Figure S2, Supporting Information). The crystal structure of the high-temperature cubic phase is shown in Figure 2c. In contrast to the arrangement in the orthorhombic phase, corner-sharing CoO_6/MoO_6 octahedra were alternately arranged along the cubic axes, forming a rock salt-type ordered double perovskite structure, as observed in Pb_2FeOsO_6.[12]

Table 3. Atomic coordinates and equivalent isotropic atomic displacement parameters of Pb_2CoMoO_6 determined by SXRD at 600 K.

Atom	Site[a)]	*x*	*y*	*z*	$100 \times U_{iso}$ [Å^2]
Pb	8*c*	0.25	0.25	0.25	2.84 (3)
Co	4*b*	0.5	0.5	0.5	2.3 (4)
Mo	4*a*	0	0	0	1.6 (2)
O1	24*e*	0.239 (2)	0	0	2.5

[a)] Space group: *Fm*-3*m* (No. 225), Z = 4, a = 8.02700(6) Å, V = 517.201(11) Å^3. R_{wp} = 5.51%, R_p = 4.17%.

© 2023 Wiley-VCH GmbH

16136829, 2024, 2, Downloaded from https://onlinelibrary.wiley.com/doi/10.1002/smll.202305219 by Institute Of Physics Chinese Academy Of Sciences, Wiley Online Library on [16/04/2024]. See the Terms and Conditions (https://onlinelibrary.wiley.com/terms-and-conditions) on Wiley Online Library for rules of use; OA articles are governed by the applicable Creative Commons License

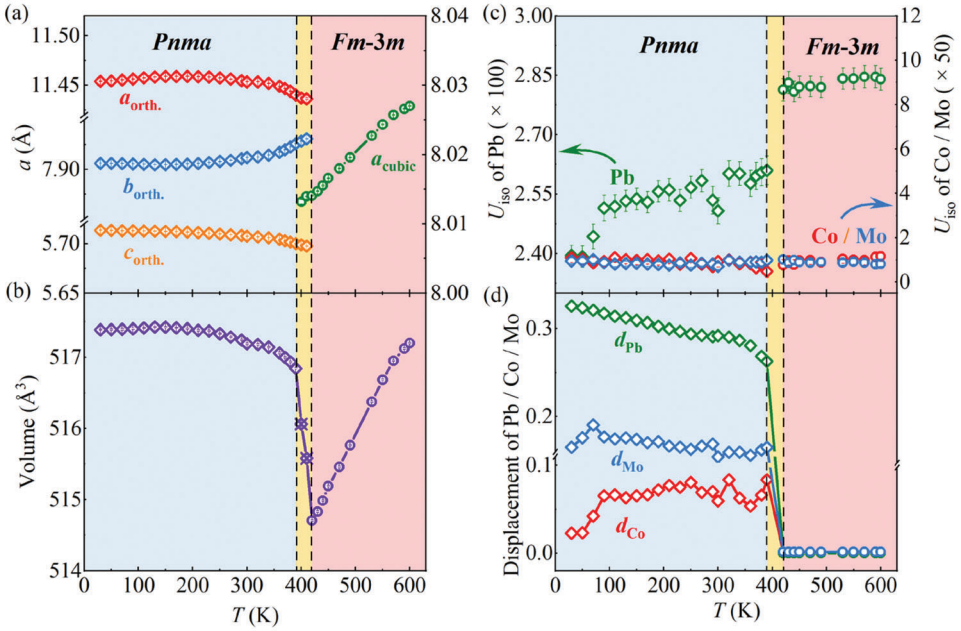

Figure 3. Temperature dependence of a) lattice parameters, b) unit cell volumes, c) atomic thermal parameters, and d) atomic displacements as determined using SXRD data for Pb_2CoMoO_6. Most error bars shown in (a–c) are within the symbols.

2.3. Antiferroelectricity of Pb_2CoMoO_6

Based on the lattice parameters of the low-temperature orthorhombic *Pnma* phase and the high-temperature cubic *Fm*-3*m* phase, it was determined that $a_{orth.} \approx \sqrt{2}a_{cubic}$, $c_{orth.} \approx \sqrt{2}/2a_{cubic}$, and $b_{orth.} \approx a_{cubic}$. This implied that the orthorhombic *Pnma* phase was formed via *ac*-plane structural distortions along the diagonal direction of the cubic *Fm*-3*m* phase. Compared to the cubic phase, in which the cations were at the coordination polyhedral centers, in the orthorhombic phase, the cations were considerably displaced away from the centers by 0.296 Å for Pb^{2+}, 0.023 Å for Co^{2+}, and 0.135 Å for Mo^{6+}. Moreover, these displacements mainly occurred in the orthorhombic *ac* plane. Figure 2d shows the schematic atomic displacements for the dominant Pb^{2+} ions in the *ac* plane. Two displacive axes were observed approximately along the cubic [100] and equivalent [001] directions as well as their opposite directions. Because the displacive atoms along each direction were equivalent, the total electric dipole moment caused by the Pb^{2+} displacement was zero in an orthorhombic unit cell. Similarly, no net dipole moment was induced by Mo^{6+} and Co^{2+} displacement. Therefore, the orthorhombic *Pnma* phase of Pb_2CoMoO_6 was determined to be antiferroelectric. To further identify the antiferroelectric structure, transmission electron microscopy (TEM) was performed at RT. Figure 2e displays the fast Fourier transform (FFT) of the high-angle annular dark-field (HAADF) image along the [010] zone axis. The observed reflections (002) and (400) are consistent with the space group of *Pnma* determined by single-crystal XRD. Figure 2f shows the HAADF image of Pb_2CoMoO_6. It is clear that the Pb atoms are considerably displaced away from the coordination polyhedral centers compared to the cubic *Fm*-3*m* phase and the displacement directions of Pb atoms are also similar to the pattern mentioned above (see Figure 2d). The TEM results thus further confirm the proposed antiferroelectric structure. Note that a polar space group $Pmc2_1$, as determined in Pb-based double perovskite Pb_2MnWO_6, was also used for the structural refinement of Pb_2CoMoO_6 (Figure S3, Supporting Information).[13] However, the resulting parameter of goodness-of-fit R_{wp} (7.32%) was larger than that fitted using the antiferroelectric *Pnma* structure (6.84%). Moreover, first-principles theoretical calculations showed that the $Pmc2_1$ phase was unstable and converged into the *Pnma* phase, further suggesting the nature of the antiferroelectric structure of Pb_2CoMoO_6 (Table S5, Supporting Information). Unfortunately, the electric field induced double ferroelectric hysteresis loops, as observed in canonical antiferroelectrics,[14] could not be detected in the present Pb_2CoMoO_6 owing to the leakage effects.

2.4. Antiferroelectricity-Induced NTE in Pb_2CoMoO_6

Next, we examined the effects of temperature on the lattice parameters and unit cell volumes of the two phases of Pb_2CoMoO_6. As shown in **Figure 3**a, for the antiferroelectric phase, the $b_{orth.}$ axis exhibited a small PTE, whereas both $a_{orth.}$ and $c_{orth.}$ axes, which are closely related to the antiferroelectric-distorted *ac* plane, displayed NTE. The calculated coefficients of thermal expansion for the lattice parameters were 8.25×10^{-6} K^{-1} for the $b_{orth.}$ axis, -4.07×10^{-6} K^{-1} for the $a_{orth.}$ axis, and -7.36×10^{-6} K^{-1} for the $c_{orth.}$ axis between 30 and 410 K. By plotting the unit cell volume as a function of temperature (Figure 3b), one found that the cell volume of Pb_2CoMoO_6 slightly decreased with increasing temperature from 30 to 390 K, and then experienced an abrupt change of −0.41% between 390 and 420 K due to the temperature-

© 2023 Wiley-VCH GmbH

16136829, 2024, 2, Downloaded from https://onlinelibrary.wiley.com/doi/10.1002/smll.202305219 by Institute Of Physics Chinese Academy Of Sciences, Wiley Online Library on [16/04/2024]. See the Terms and Conditions (https://onlinelibrary.wiley.com/terms-and-conditions) on Wiley Online Library for rules of use; OA articles are governed by the applicable Creative Commons License

induced first-order antiferroelectric-to-paraelectric phase transition. Therefore, in addition to the ferroelectric-to-paraelectric and ferroelectric-to-antiferroelectric transitions, an antiferroelectric-to-paraelectric phase transition can also induce NTE. Consequently, a new NTE mechanism, that is, antiferroelectricity-induced NTE, was proposed for the first time in Pb_2CoMoO_6. Besides, the value of α_V was calculated as -1.33×10^{-5} K^{-1} in a wide temperature region of 30–420 K. Such a remarkable negative α_V suggested that Pb_2CoMoO_6 exhibited NTE in its antiferroelectric phase. In sharp contrast, however, the cubic paraelectric phase exhibited normal PTE with $\alpha_V = 2.70 \times 10^{-5}$ K^{-1} at 420–600 K. Note that the negative value of α_V for the antiferroelectric Pb_2CoMoO_6 is comparable to that of the well-known ferroelectric NTE material $PbTiO_3$ ($\alpha_V = -1.99 \times 10^{-5}$ K^{-1}, 298–763 K).[15]

Usually, when a material has a small α_V value between −2 and 2×10^{-6} K^{-1}, it can be regarded as a ZTE material.[16] Since the thermal expansion or contraction effect is negligible during heating or cooling, the ZTE material is favorable for practical applications. If one only considered the temperature range of 30–360 K, the negative value of α_V (-1.92×10^{-6} K^{-1}) for the antiferroelectric Pb_2CoMoO_6 was quite small, and the compound is a promising candidate for a ZTE material with the working temperatures across RT. Furthermore, if we focused on a lower-temperature window of 30–250 K, the current Pb_2CoMoO_6 exhibited an ultralow value of $\alpha_V = -4.92 \times 10^{-7}$ K^{-1}. This value was comparable to that of the best low-temperature ZTE material reported thus far, that is, nano-sized $Mn_3Cu_{0.5}Ge_{0.5}N$ with $\alpha_V = 3.54 \times 10^{-7}$ at 12–230 K.[1a,b,3b]

Figure 3c shows the temperature dependence of thermal parameters of Pb, Co, and Mo atoms refined from the temperature-dependent SXRD data. The thermal parameter of Pb just slightly changed in the cubic paraelectric phase, whereas it underwent a sharp decrease when the structural phase transition occurred toward the antiferroelectric phase. This was reminiscent of the off-center displacements caused by the lone-pair ions like Pb^{2+} and Bi^{3+} as observed in some ferroelectrics during the paraelectric-to-ferroelectric phase transitions.[17] In comparison, the thermal parameters of Co and Mo nearly remained constant in the whole temperature region we measured (30–600 K). These features indicated that the antiferroelectric displacement of Pb might trigger the structural phase transition in Pb_2CoMoO_6. Figure 3d shows the temperature dependence of atomic displacements for Pb, Co, and Mo across the phase transition. Obviously, Pb atoms exhibited the largest value of displacement compared with those of Co and Mo. Moreover, the atomic displacement of Pb (d_{Pb}) in the antiferroelectric phase apparently decreased upon heating. However, the displacements of Co (d_{Co}) and Mo (d_{Mo}) remained little changed. One thus concluded that the off-center antiferroelectric displacement of Pb would dominate the occurrence of NTE in the current Pb_2CoMoO_6.

3. Conclusion

In summary, we successfully synthesized high-quality single crystals and polycrystalline samples of B-site-ordered double perovskite Pb_2CoMoO_6 at high pressure and temperature conditions. Single-crystal XRD and powder SXRD results indicated that Pb_2CoMoO_6 crystallized into an orthorhombic antiferroelectric *Pnma* phase at RT. A temperature-induced first-order structural phase transition from the orthorhombic *Pnma* phase to the cubic paraelectric *Fm*-3*m* phase was observed at ≈400 K. A comparison of the structures of the two phases showed that the antiferroelectricity was dominated by the opposite displacements of Pb^{2+} ions. Unexpectedly, Pb_2CoMoO_6 experienced a sharp volume contraction of 0.41% during the antiferroelectric-to-paraelectric phase transition and even exhibited remarkable NTE in a wide temperature region of 30–420 K with $\alpha_V = -1.33 \times 10^{-5}$ K^{-1}. Therefore, an antiferroelectricity-induced NTE was established for the first time. The as-prepared Pb_2CoMoO_6 serves as a unique material for studying antiferroelectricity-induced NTE based on a new mechanism.

4. Experimental Section

Materials Synthesis: High-purity PbO (99.999%, Aladdin), CoO (99.995%, Alfa), and MoO_3 (99.998%, Alfa) powders were thoroughly mixed and ground at a molar ratio of 2:1:1 in a glovebox filled with argon. The mixed powders were sealed in a gold capsule of 3.0 mm diameter and 5.0 mm height. The capsule was treated at 6.0 GPa and 1273 K for 30 min using a cubic anvil-type high-pressure apparatus. The sample was then quenched to room temperature (RT), and the pressure was gradually released to attain ambient pressure over 3.0 h. Polycrystalline Pb_2CoMoO_6 was thus obtained using these procedures. Pb_2CoMoO_6 single crystals with a size of ≈200 µm were also prepared by performing the synthesis reaction at 1373 K and 6.0 GPa for 2.0 h.

Crystallographic Characterization: Temperature-dependent synchrotron X-ray diffraction (SXRD) was performed using a large Debye–Scherrer camera installed at the beamline BL02B2 (λ = 0.41987 Å) of SPring-8.[18] X-ray diffraction (XRD) was performed using a Rigaku SmartLab diffractometer with Cu *Kα* radiation (λ = 1.54059 Å, 45 kV, and 200 mA) in the 2θ range from 10 to 100° with steps of 0.01°. The GSAS software was used for powder SXRD Rietveld refinement.[19] Single-crystal X-ray diffraction (XRD) data were collected using a Bruker D8 VENTURE PHOTO II diffractometer with multilayer-mirror-monochromatized Mo K_α (λ = 0.71073 Å) radiation at RT. Unit-cell refinement and data reduction were performed using the APEX software.[20] The collected data were corrected for absorption effects using the multi-scan method and refined via the full-matrix least-squares method based on F^2 using the Bruker SHELXTL software package.[21]

X-Ray Absorption Spectroscopy: X-ray absorption spectroscopy (XAS) at the Co-$L_{2,3}$ and Mo-L_3 edges was performed at the BL11A and TLS16A beamlines of the National Synchrotron Radiation Research Center, Taiwan. The high-resolution partial fluorescence yield Pb-L_3 XAS spectra with an overall resolution of ≈1.0 eV were measured at the ID 20 beamline of the European Synchrotron Radiation Facility (France).

Differential Scanning Calorimetry: Differential scanning calorimetry (DSC) measurements were performed using a DSC131 Evo thermal analyzer under an argon atmosphere with heating and cooling rates of 5 K min^{-1}.

Transmission Electron Microscopy: The aberration-corrected transmission electron microscopy (TEM) and scanning transmission electron microscopy (STEM) experiments were performed on a JEOL ARM200F transmission electron microscope equipped with double Cs correctors (CEOS) for the condenser lens and objective lens. Annular bright-field (ABF) and high-angle annular dark-field (HAADF) images were acquired at acceptance angles of 11.5–23.0 and 90–370 mrad, respectively. The available spatial resolution for each of the STEM images was better than 78 pm at 200 kV.

First-Principles Theoretical Calculations: All calculations were performed based on the density functional theory (DFT) within the Vienna abinitio simulation package (VASP), with the projector augmented wave

© 2023 Wiley-VCH GmbH

16136829, 2024, 2, Downloaded from https://onlinelibrary.wiley.com/doi/10.1002/smll.202305219 by Institute Of Physics Chinese Academy Of Sciences, Wiley Online Library on [16/04/2024]. See the Terms and Conditions (https://onlinelibrary.wiley.com/terms-and-conditions) on Wiley Online Library for rules of use; OA articles are governed by the applicable Creative Commons License

(PAW) potentials to describe the electron-ionic core interaction.[22] The Perdew–Burke–Ern-zerhof (PBE) formulation of the generalized gradient approximation (GGA) was chosen to describe the exchange-correlation interaction of electrons and the wave functions were expanded in a plane-wave basis set with an energy cut-off of 650 eV for structural relaxation and 550 eV for electronic structure.[23] The force on each ion was converged to be less than 0.001 eV $Å^{-1}$ and all the geometric structures were fully relaxed to minimize the total energy of the system until a precision of 10^{-6} eV was reached. The Pb $5d^{10}6s^26p^2$, Mo $4p^64d^55s^1$, Co $3p^63d^74s^2$, and O $2s^22p^4$ electrons were treated as valence electrons. The *k* spacing of 0.02 $Å^{-1}$ grid in reciprocal space was used to ensure the convergence for the total energy self-consistent calculations.

Supporting Information

Supporting Information is available from the Wiley Online Library or from the author.

Acknowledgements

This work was supported by the National Key Research and Development Program of China (Grant No. 2021YFA1400300), the Beijing Natural Science Foundation (Grant No. Z200007), the National Natural Science Foundation of China (Grant Nos. 11934017, 12261131499, 11921004, 22171283, and 12204515), the Chinese Academy of Sciences (Grant No. XDB33000000), JSPS KAKENHI (Grant Nos. JP18H05208 and JP19H05625), and JST-CREST (JPMJCR22O1). The synchrotron radiation experiments were conducted at SPring-8 with the approval of the Japan Synchrotron Radiation Research Institute (Proposal Numbers 2022B1852). The authors acknowledge support from the Max Planck-POSTECH-Hsinchu Center for Complex Phase Materials.

Conflict of Interest

The authors declare no conflict of interest.

Data Availability Statement

The data that support the findings of this study are available from the corresponding author upon reasonable request.

Keywords

antiferroelectricity, double perovskites, high-pressure synthesis, negative thermal expansion

Received: June 22, 2023
Revised: August 18, 2023
Published online: September 1, 2023

[1] a) Q. Li, K. Lin, Z. Liu, L. Hu, Y. Cao, J. Chen, X. Xing, *Chem. Rev.* **2022**, *122*, 8438; b) J. Chen, L. Hu, J. Deng, X. Xing, *Chem. Soc. Rev.* **2015**, *44*, 3522; c) P. Mohn, *Nature* **1999**, *400*, 18; d) A. Atkinson, S. Barnett, R. J. Gorte, J. T. Irvine, A. J. McEvoy, M. Mogensen, S. C. Singhal, J. Vohs, *Nat. Mater.* **2004**, *3*, 17; e) W. Miller, C. W. Smith, D. S. Mackenzie, K. E. Evans, *J. Mater. Sci.* **2009**, *44*, 5441; f) T. A. Mary, J. S. O. Evans, T. Vogt, A. W. Sleight, *Science* **1996**, *272*, 90; g) K. Takenaka, *Sci. Technol. Adv. Mater.* **2012**, *13*, 013001; h) R. Huang, Y. Liu, W. Fan, J. Tan, F. Xiao, L. Qian, L. Li, *J. Am. Chem. Soc.* **2013**, *135*, 11469; i) D. Das, T. Jacobs, L. J. Barbour, *Nat. Mater.* **2010**, *9*, 36.

[2] a) Z. Pan, J. Chen, X. Jiang, Z. Lin, L. Zhang, L. Fan, Y. Rong, L. Hu, H. Liu, Y. Ren, X. Kuang, X. Xing, *Inorg. Chem.* **2017**, *56*, 2589; b) M. Xu, Y. Song, Y. Xu, Q. Sun, F. Long, N. Shi, Y. Qiao, C. Zhou, Y. Ren, J. Chen, *Chem. Mater.* **2022**, *34*, 9437; c) L. Hu, J. Chen, L. Fan, Y. Ren, Y. Rong, Z. Pan, J. Deng, R. Yu, X. Xing, *J. Am. Chem. Soc.* **2014**, *136*, 13566; d) J. Chen, X. Xing, C. Sun, P. Hu, R. Yu, X. Wang, L. Li, *J. Am. Chem. Soc.* **2008**, *130*, 1144.

[3] a) S. E. Tallentire, F. Child, I. Fall, L. Vella-Zarb, I. R. Evans, M. G. Tucker, D. A. Keen, C. Wilson, J. S. Evans, *J. Am. Chem. Soc.* **2013**, *135*, 12849; b) X. Song, Z. Sun, Q. Huang, M. Rettenmayr, X. Liu, M. Seyring, G. Li, G. Rao, F. Yin, *Adv. Mater.* **2011**, *23*, 4690; c) J. Liu, H. E. Maynard-Casely, H. E. A. Brand, N. Sharma, *Chem. Mater.* **2021**, *33*, 3823.

[4] S. Margadonna, K. Prassides, A. N. Fitch, *J. Am. Chem. Soc.* **2004**, *126*, 15390.

[5] M. van Schilfgaarde, I. A. Abrikosov, B. Johansson, *Nature* **1999**, *400*, 46.

[6] a) Z. Pan, J. Chen, X. Jiang, L. Hu, R. Yu, H. Yamamoto, T. Ogata, Y. Hattori, F. Guo, X. Fan, Y. Li, G. Li, H. Gu, Y. Ren, Z. Lin, M. Azuma, X. Xing, *J. Am. Chem. Soc.* **2017**, *139*, 14865; b) H. Yamamoto, T. Imai, Y. Sakai, M. Azuma, *Angew. Chem., Int. Ed.* **2018**, *57*, 8170; c) T. Nishikubo, T. Imai, Y. Sakai, M. Mizumaki, S. Kawaguchi, N. Oshime, A. Shimada, K. Sugawara, K. Ohwada, A. Machida, T. Watanuki, K. Kurushima, S. Mori, T. Mizokawa, M. Azuma, *Chem. Mater.* **2023**, *35*, 870.

[7] a) M. Azuma, W. T. Chen, H. Seki, M. Czapski, S. Olga, K. Oka, M. Mizumaki, T. Watanuki, N. Ishimatsu, N. Kawamura, S. Ishiwata, M. G. Tucker, Y. Shimakawa, J. P. Attfield, *Nat. Commun.* **2011**, *2*, 347; b) Y. W. Long, N. Hayashi, T. Saito, M. Azuma, S. Muranaka, Y. Shimakawa, *Nature* **2009**, *458*, 60; c) E. Pachoud, J. Cumby, C. T. Lithgow, J. P. Attfield, *J. Am. Chem. Soc.* **2018**, *140*, 636.

[8] J. Chen, F. Wang, Q. Huang, L. Hu, X. Song, J. Deng, R. Yu, X. Xing, *Sci. Rep.* **2013**, *3*, 2458.

[9] a) G. A. Rossetti, J. P. Cline, A. Navrotsky, *J. Mater. Res.* **1998**, *13*, 3197; b) G. Shirane, *Phys. Rev.* **1952**, *86*, 219; c) G. Rujijanagul, T. Bongkarn, *Phase Transitions* **2007**, *80*, 209.

[10] a) V. A. Isupov, *Ferroelectrics* **2011**, *289*, 131; b) T. Fujita, O. Fukunaga, T. Nakagawa, S. Nomura, *Mater. Res. Bull.* **1970**, *5*, 759; c) K. P. Burdina, L. G. Sev-astyanova, E. V. Zubova, Y. N. Venevtsev, *Izv. AN SSSR, ser. fiz.* **1975**, *39*, 1095.

[11] V. M. Egorov, V. V. Lemanov, *Phys. Solid State* **2006**, *48*, 1954.

[12] Q. Zhao, M. Liu, J. Dai, H. Deng, Y. Yin, L. Zhou, J. Yang, Z. Hu, S. Agrestini, K. Chen, E. Pellegrin, M. Valvidares, L. Nataf, F. Baudelet, L. H. Tjeng, Y. F. Yang, C. Jin, Y. Long, *Inorg. Chem.* **2016**, *55*, 9816.

[13] F. Orlandi, L. Righi, R. Cabassi, D. Delmonte, C. Pernechele, F. Bolzoni, F. Mezzadri, M. Solzi, M. Merlini, G. Calestani, *Inorg. Chem.* **2014**, *53*, 10283.

[14] C. A. Randall, Z. Fan, I. Reaney, L. Q. Chen, S. Trolier-McKinstry, *J. Am. Ceram. Soc.* **2021**, *104*, 3775.

[15] J. Chen, X. Xing, R. Yu, G. Liu, *J. Am. Ceram. Soc.* **2005**, *88*, 1356.

[16] M. J. Dejneka, C. L. Chapman, S. T. Misture, D. J. Green, *J. Am. Ceram. Soc.* **2011**, *94*, 2249.

[17] a) L. Zhou, J. Dai, Y. Chai, H. Zhang, S. Dong, H. Cao, S. Calder, Y. Yin, X. Wang, X. Shen, Z. Liu, T. Saito, Y. Shimakawa, H. Hojo, Y. Ikuhara, M. Azuma, Z. Hu, Y. Sun, C. Jin, Y. Long, *Adv. Mater.* **2017**, *29*, 1703435; b) A. K. Singh, A. K. Singh, *Solid State Sci.* **2012**, *14*, 100; c) M. Bonin, W. Paciorek, K. J. Schenk, G. Chapuis, *Acta Crystallogr., Sect. B: Struct. Sci., Cryst. Eng. Mater.* **1995**, *51*, 48.

[18] S. Kawaguchi, M. Takemoto, K. Osaka, E. Nishibori, C. Moriyoshi, Y. Kubota, Y. Kuroiwa, K. Sugimoto, *Rev. Sci. Instrum.* **2017**, *88*, 085111.

[19] A. C. Larson, R. B. Dreele, B. Toby, General Structure Analysis System – GSAS/EXPGUI, **1994**, *748*.

© 2023 Wiley-VCH GmbH

16136829, 2024, 2, Downloaded from https://onlinelibrary.wiley.com/doi/10.1002/smll.202305219 by Institute Of Physics Chinese Academy Of Sciences, Wiley Online Library on [16/04/2024]. See the Terms and Conditions (https://onlinelibrary.wiley.com/terms-and-conditions) on Wiley Online Library for rules of use; OA articles are governed by the applicable Creative Commons License

[20] DOC-M86-EXX229 APEX3 Software User Manual Bruker AXS Inc, Madison, Wisconsin **2016**.
[21] G. M. Sheldrick, *Acta Crystallogr., Sect. C: Struct. Chem.* **2015**, *71*, 3.
[22] a) G. Kresse, J. Furthmuller, *Comput. Mater. Sci.* **1996**, *6*, 15; b) G. Kresse, J. Furthmuller, *Phys. Rev. B* **1996**, *54*, 11169, c) G. Kresse, D. Joubert, *Phys. Rev. B* **1999**, *59*, 1758.
[23] J. P. Perdew, K. Burke, M. Ernzerhof, *Phys. Rev. Lett.* **1996**, *77*, 3865.

© 2023 Wiley-VCH GmbH

16136829, 2024, 2, Downloaded from https://onlinelibrary.wiley.com/doi/10.1002/smll.202305219 by Institute Of Physics Chinese Academy Of Sciences, Wiley Online Library on [16/04/2024]. See the Terms and Conditions (https://onlinelibrary.wiley.com/terms-and-conditions) on Wiley Online Library for rules of use; OA articles are governed by the applicable Creative Commons License